

Low-Cycle-Fatigue Performance of Stress-Aged EN AW-7075 Alloy

Seyed Vahid Sajadifar,* Philipp Krooß, Marcel Krochmal, Thomas Wegener, Akbar Heidarzadeh, Hannes Fröck, Janez Zavašnik, Olaf Kessler, and Thomas Niendorf

The effect of a novel heat treatment, that is, aging under superimposed external stress, on the fatigue performance and microstructural evolution of a high-strength aluminum alloy (EN AW-7075) is presented. Stress aging, a combination of heat treatment and superimposed external stress, can enhance the mechanical properties of EN AW-7075 under monotonic loading due to the acceleration of precipitation kinetics. Scanning electron microscopy (SEM) and scanning transmission electron microscopy (STEM) reveal that a longer aging time and the presence of superimposed stress both promote the formation and growth of precipitates, that is, the precipitation of strengthening η' precipitates. This is confirmed by differential scanning calorimetry (DSC) heating experiments of stressless and stress-aged states. Furthermore, stress aging leads to a reduction of dimensions of precipitate-free zones near grain boundaries. Cyclic deformation responses (CDRs) and half-life hysteresis loops are evaluated focusing on the low-cycle fatigue (LCF) performance of different conditions. A noticeable cyclic hardening seen in case of the specimens aged for a short time indicates the occurrence of dynamic strain aging (DSA). Eventually, stress aging allows for an enhancement of the monotonic mechanical properties of EN AW-7075 without degrading the cyclic performance in the LCF regime.

lightweight alloys can lead to a decrease in fuel consumption and CO₂ emissions.^[2] Recently, many research works have been focused on high-strength aluminum (Al) alloys as a potential substitute for steels.^[3–5] Different series of high-strength Al alloys with various alloying elements were developed to widen their utilization.^[6–8] Among them, the EN AW-7075 alloy exhibits outstanding mechanical properties and good workability.^[9] Resulting from a combination of excellent mechanical properties as well as a high strength-to-weight ratio, EN AW-7075 was found to be a promising candidate for lightweight parts in aerospace and automotive industries.^[2,4,10,11]

The mechanical properties of EN AW-7075 alloy can be modified by heat- and thermomechanical treatment,^[12–14] and various procedures were developed for tuning of the mechanical properties depending on different requirements of numerous applications.^[15,16] Recently, novel thermomechanical treatments were employed to further improve the mechanical behavior


of EN AW-7075 alloy.^[12–14,17] Stress aging was found to be capable of enhancing the mechanical properties.^[17,18] Previous studies showed that external stress or strains induced during aging considerably accelerate the precipitation kinetics,^[17,18] as this approach can provide additional nucleation sites for precipitates.^[19,20]

1. Introduction

The development of lightweight structural materials as a response to the global warming problem and its detrimental influence on the environment has lately drawn great attention.^[1] The replacement of conventional iron-based metals with

S. V. Sajadifar, P. Krooß, M. Krochmal, T. Wegener, T. Niendorf
Institute of Materials Engineering
University of Kassel
Mönchebergstraße 3, 34125 Kassel, Germany
E-mail: sajjadifar@uni-kassel.de

A. Heidarzadeh
Department of Materials Engineering
Azarbaijan Shahid Madani University
Tabriz 53714-161, Iran

 The ORCID identification number(s) for the author(s) of this article can be found under <https://doi.org/10.1002/adem.202300090>.

© 2023 The Authors. Advanced Engineering Materials published by Wiley-VCH GmbH. This is an open access article under the terms of the Creative Commons Attribution License, which permits use, distribution and reproduction in any medium, provided the original work is properly cited.

DOI: 10.1002/adem.202300090

H. Fröck, O. Kessler
Chair of Materials Science
University of Rostock
Albert-Einstein-Str. 2, 18059 Rostock, Germany

J. Zavašnik
Max-Planck-Institut für Eisenforschung
Max-Planck-Str. 1, 40237 Düsseldorf, Germany

J. Zavašnik
Gaseous Electronics
Jožef Stefan Institute
Jamova 39, SI-1000 Ljubljana, Slovenia

O. Kessler
Competence Centre CALOR
Department of Life, Light and Matter
University of Rostock
Albert-Einstein-Str. 25, 18059 Rostock, Germany

The variation of aging temperature, aging time, and external stress directly influences the nucleation and growth of second-phase precipitates in high-strength Al alloys.^[19,20] Accordingly, different heat treatments lead to different precipitates in the EN AW-7075 alloy.^[21] The precipitation sequence during aging treatment of a supersaturated solid solution (SSS) in this alloy is: SSS → Guinier-Preston (GP) zones → η' (MgZn) → η (MgZn₂ or Mg(Cu_xZn_{1-x})₂). Schematics related to nucleation of different precipitates with varying aging temperatures, durations, and cooling rates from solution heat treatment were presented in a recent work published by some of the present authors.^[17] It is well known that GP zones and η' precipitates can considerably improve the strength of EN AW-7075 alloy, while coarse η precipitates detrimentally affect the hardening of this alloy.^[22,23] Additionally, during the growth of coarse η precipitates, the flux of solute atoms toward formed precipitates occurs, resulting in the depletion of alloying elements in the vicinity of coarse precipitates and eventually the formation of precipitate-free zones (PFZs) in the microstructure.^[12,14] It was reported that these PFZs can adversely affect the mechanical properties of EN AW-7075 alloy.^[24]

The precipitation process in Al alloys can successfully be analyzed in situ using differential scanning calorimetry (DSC) at various temperatures and scanning rates.^[17,25] During heating of precipitation-hardened Al alloys in solution-heat-treated and quenched condition, second-phase particles are formed and dissolved according to the temperature changes. Dissolution and precipitation in Al alloys can be distinguished as endothermic and exothermic peaks, respectively.^[26] Several researchers concentrated on the assessment of second-phase particles formed during stress aging treatment using DSC measurements.^[17,27–29] Results indicate that DSC is a powerful tool for characterizing precipitates formed upon stress aging. Previously, DSC measurements confirmed that the enhancement in the strength of the EN AW-7075 alloy induced via aging under stress is connected to the increased fraction of strengthening η' precipitates formed.^[17]

Numerous components are subjected to cyclic loading while in service; hence, investigating the fatigue performance of parts is essential. Several studies concentrated on the fatigue performance of high-strength Al alloys.^[30–35] Most recently, a few studies focused on the cyclic response of a thermomechanically treated EN AW-7075 alloy.^[36–38] An enhancement in the crack nucleation resistance due to grain refinement was found in this alloy, while the ultrafine-grained microstructure was prone to crack propagation.^[37] Low-cycle fatigue (LCF) behavior of parts thermomechanically treated with different temperatures was further studied.^[36] Accordingly, components formed with temperatures below 200 °C exhibited an excellent cyclic response.

Up to now, only a few investigations have studied the impact of second-phase particle type and morphology on the cyclic deformation responses (CDRs) of thermomechanically treated Al alloys.^[36–38] As discussed earlier, stress aging of high-strength Al alloys as a novel thermomechanical treatment can alter the

microstructure and, thus, influence the mechanical properties of these alloys under cyclic loading. To the best of the authors' knowledge, the CDR of stress-aged EN AW-7075 alloy has not been studied yet. Therefore, the present study aims to close this research gap by exploring the mechanical properties of stress-aged EN AW-7075 alloy under cyclic loading. Data acquired can be employed to establish relationships between stress response, fatigue life, and the microstructural evolution of the high-strength Al parts upon stress aging. In this regard, fatigue performance and microstructural evolution of this alloy upon stress aging are discussed by analysis of CDRs, Masing behavior, as well as related microstructural investigations.

2. Experimental Section

2.1. Materials

The as-received material was present in form of EN AW-7075 bars with a diameter of 15 mm and a length of 3000 mm. The material was received in peak aged (T6) condition. The chemical composition (in wt%) of the as-received material was analyzed by optical emission spectroscopy (OES) and is summarized in **Table 1**. It agrees with the specification according to the standard EN 573-3.

2.2. Stress Aging Treatment

Similar to a previous study,^[17] cylindrical dogbone-shaped specimens with dimensions shown in **Figure 1b** were machined from the as-received bars. The cylindrical specimens were first solution heat treated in a furnace at 480 °C for 30 min, followed by water quenching. Then, specimens were aged at 120 °C for 2 h and 24 h under 0 MPa (load free) and 200 MPa (cf. **Figure 1c, d**). Temperatures were measured using a thermocouple in contact with the surface of the cylindrical specimens attached by steel springs. Stress and strain values were monitored by a load cell and extensometer, respectively. From these stress-aged specimen, miniature LCF specimens were manufactured according to **Figure 1a**.

2.3. Characterization of Mechanical Properties

Monotonic mechanical properties of different conditions were characterized by uniaxial tensile experiments at room temperature using a screw-driven MTS Criterion load frame with a maximum loading capability of 20 kN under displacement control with a constant crosshead speed of 2 mm min⁻¹. Strain values were measured by an extensometer. For each condition, three repetitions were carried out. Strain-controlled LCF tests under fully reversed push-pull loading ($R = -1$) were conducted employing a digitally controlled servohydraulic load frame with

Table 1. Chemical composition of the alloy determined via OES.

Element	Si	Fe	Cu	Mn	Mg	Cr	Zn	Ti	Zr	Al
EN AW-7075 [wt%]	0.08	0.13	1.40	0.03	2.30	0.20	5.50	0.02	0.05	Balance

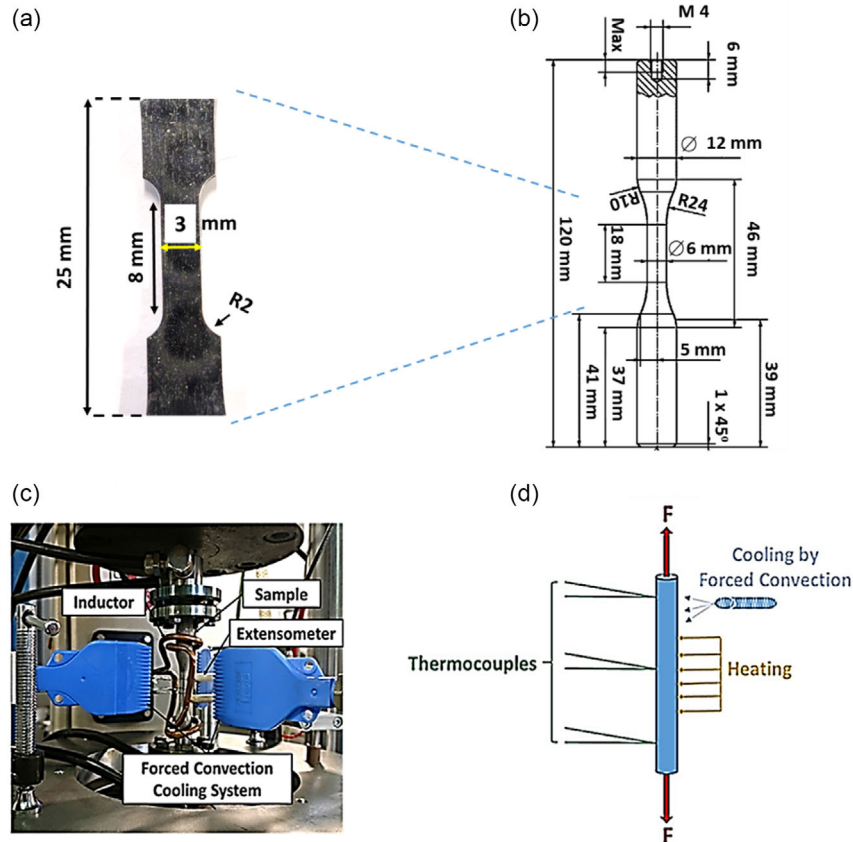


Figure 1. a) Miniature flat specimen electron discharge machined from the cylindrical specimen for LCF experiments, b) cylindrical dogbone specimens utilized for stress aging, c) photograph displaying the stress aging setup, and d) schematic highlighting the process (Reproduced under terms of the CC-BY license.^[17] Copyright 2022, S.V. Sajadifar et al., published by Metals).

a maximum force capability of 16 kN at total strain amplitudes of $\Delta\epsilon_t/2 = \pm 0.4\%$, $\Delta\epsilon_t/2 = \pm 0.6\%$, and $\Delta\epsilon_t/2 = \pm 0.8\%$ and a constant strain rate of 0.006 s^{-1} . A MTS miniature extensometer featuring a gauge length of 5 mm directly attached to the specimen surface was used to measure and control the strain values during the LCF experiments. Vickers hardness measurements were conducted on the specimens by application of 29.4 N (HV3) for 15 s at ambient temperature. A Struers hardness tester was employed for the hardness measurements.

2.4. Analysis of Microstructure

The microstructures of the material in different conditions were studied by backscattered electron (BSE) imaging mode in a high-resolution scanning electron microscope (SEM, Zeiss ULTRA

GEMINI, Germany) operated at 20 kV. All measurements were performed at the same working distance and magnification, that is, 9 mm and $10\times$, respectively. For BSE analysis, specimens were gradually mechanically ground down to 4000 grit size using SiC abrasive papers followed by polishing in colloid silica polishing suspension. Morphology and fracture surfaces were analyzed using the secondary electron (SE) imaging mode (SEM, CamScan MV 2300, Electron Optic Services).

The microstructure and chemistry of materials in different conditions on the nanolevel were further studied using a scanning transmission electron microscope (STEM, ARM-20^{CF}, JEOL Inc.) operated at 200 kV and equipped with a high-angle-annular dark-field detector (HAADF, Gatan Inc.) and energy-dispersive X-Ray spectrometer (EDS, Centurion large angle SDD, JEOL Inc.). The electron-transparent specimens

Table 2. Tensile and hardness properties of EN AW-7075 alloy in various conditions. Standard deviations are reported in the table.

Conditions	T6	120 °C_2 h_0 MPa	120 °C_24 h_0 MPa	120 °C_2 h_200 MPa	120 °C_24 h_200 MPa
Hardness [HV 3]	170.3 ± 2.8	151.3 ± 2.8	166.5 ± 3.8	158.7 ± 2.6	171.7 ± 3.9
YS [MPa]	448.7 ± 3.4	397.0 ± 2.8	431.2 ± 2.4	401.2 ± 9.1	451.1 ± 3.9
UTS [MPa]	577.2 ± 4.2	541.1 ± 3.2	554.6 ± 5.2	542.6 ± 7.7	579.45 ± 2.9
A [%]	8.2 ± 0.9	12 ± 0.1	14.4 ± 1.4	13.1 ± 0.9	10.3 ± 1.1

taken from the fatigued conditions for STEM studies were prepared by punching 3 mm disks from regions close to the edge of the fracture surface to analyze the area being characterized by the highest accumulated cyclic strain. The disks were mechanically thinned to 60 μm (Disc Grinder Mod. 623, Gatan Inc.) and dimpled to 5 μm at the disk center (dimple grinder Mod. 656, Gatan Inc.). The specimens were ion milled by a precision ion-polishing system (PIPS Mod. 691, Gatan Inc.) at 4.5 keV and an incident angle of 8° until perforation.

2.5. Differential Scanning Calorimetry

DSC heating experiments were performed and evaluated as described in another study.^[39] The DSC measurements were performed using a Perkin-Elmer Pyris 8500 calorimeter equipped with a Huber TC 125 W MT cooler. Nitrogen gas was purged to provide an inert atmosphere. To prevent the measuring device from icing and to keep a constant ambient condition, the device was located under an acrylic glass box, this box being flushed with dry air. DSC measurements were performed on specimens

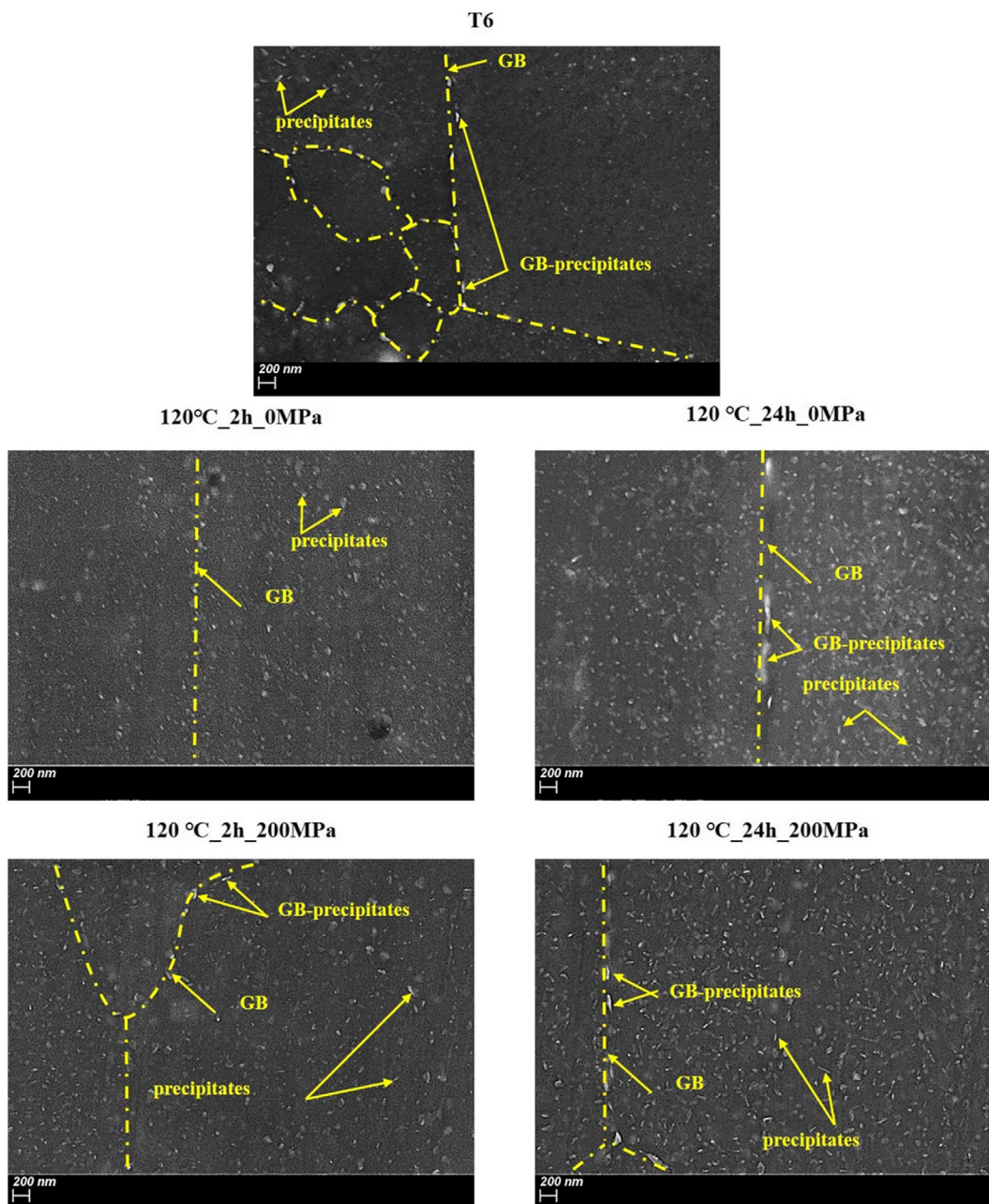


Figure 2. BSE images of the as-received, conventionally, and stress-aged specimens; images were taken at the same magnification. Selected GBs and precipitates are marked by dash-dotted yellow lines and yellow arrows, respectively. GB precipitates and precipitates in the grain interior were observed in all conditions.

$\varnothing 6 \times 1$ mm, which were manufactured from the gauge lengths of stress-aged specimens (Figure 1b). DSC samples were placed in pure Al crucibles and covered with pure Al lids. The specimens had masses of about 80 mg. Pure Al specimens of similar mass were used as reference specimens. Heating was conducted from 30 °C to 490 °C at a constant rate of 1 K s⁻¹. Four individual measurements and two baseline measurements were recorded for each condition. In Section 3, the mean curve obtained from the individual DSC measurements is shown.

3. Results and Discussion

3.1. Mechanical Properties Under Monotonic Loading

Mechanical properties of conventionally and stress-aged specimens under monotonic loading are summarized in Table 2. Hardness and tensile results were comprehensively discussed in a previous research work by some of the present authors.^[17] Here, the mechanical properties of conventionally and stress-aged EN AW-7075 are briefly summarized. Regardless of external stress, aging of this alloy for a longer time increases yield strength (YS), ultimate tensile strength (UTS), and hardness. At longer aging times, solute atoms have enough time to diffuse from SSS to form strengthening precipitates, for example, η' .^[40] It is also worth noting that higher hardness, YS, and UTS values were obtained with external stress during aging. External stress/strain during aging results in dislocation multiplication and, thus, additional nucleation sites facilitating precipitation.^[19]

3.2. Microstructural Evolution upon Stress Aging

The BSE images of EN AW-7075 alloy in different conditions are shown in Figure 2; grain boundaries (GBs) are highlighted by dash-dotted yellow lines for better visibility. As can be observed, GB precipitates are present in all conditions examined. Coarse precipitates along the GBs and in the grain interior presumably represent the η phase.^[41] Some coarse precipitates may be quench-induced precipitates and some may form during aging of the SSS for a long time.^[42] Such coarse precipitates can hardly improve the strength of EN AW-7075 alloy since they result in a large interparticle spacing and eventually easy movements of dislocations.^[21] It must be noted that precipitates formed within the grain interior are coarser for the specimens aged for 24 h compared to those aged for 2 h. The growth of precipitates with the increase in aging duration is connected to the sufficiency of time for diffusion of alloying elements toward second-phase particles.^[40] From the BSE images shown, the effect of external stress during aging on the size and morphology of precipitates can hardly be discussed. Therefore, transmission electron microscopy (TEM) studies (shown in the following section) were carried out to fully understand the effect of superimposed stress during aging on microstructural evolution.

The DSC heating curves of specimens aged with and without the presence of external stress are shown in Figure 3. A sequence of endothermal dissolution and exothermal precipitation reaction occurs, which, according to ref. [17], can be correlated with certain transformations: dissolution of GP-zones (A), dissolution

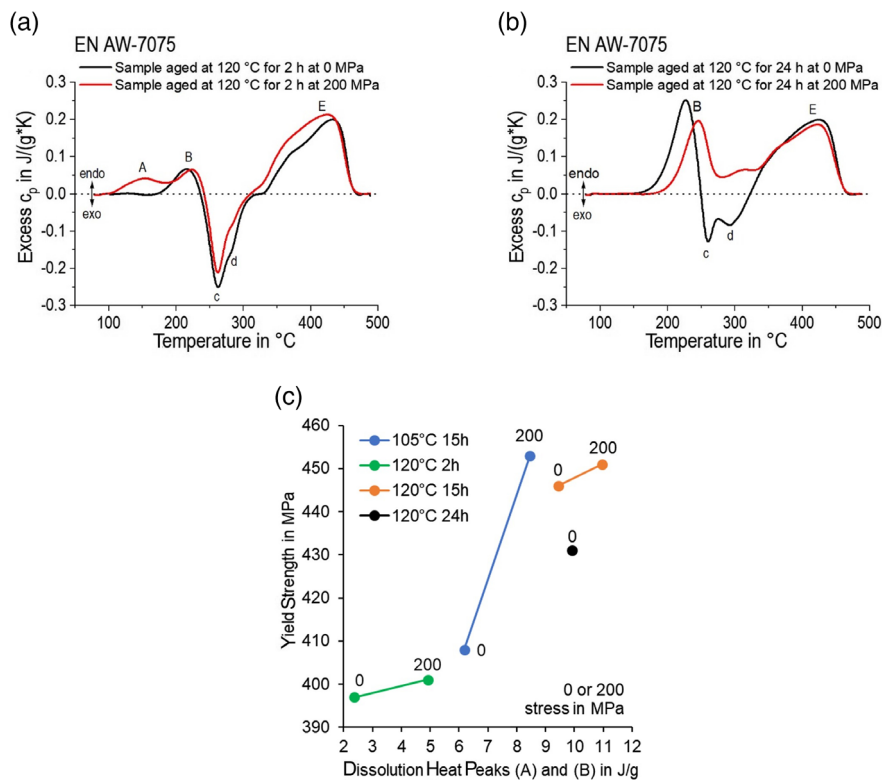


Figure 3. DSC heating experiments on specimen aged at 120 °C with and without the presence of external stress of 200 MPa: a) 120 °C 2 h, b) 120 °C 24 h, and c) correlation between dissolution heat and YS.

of η' (B), precipitation of η -Zn₂Mg (c + d), and dissolution of η (E). Stress aging at 200 MPa and 120 °C for 2 h causes a significantly larger peak A compared to stressless aging (Figure 3a). More strengthening GP zones have been formed during stress aging. A similar behavior can be observed for stress aging of 200 MPa at 120 °C for 24 h (Figure 3b). In this case, dissolution and precipitation reactions strongly overlap, and the cumulative DSC curve is shifted to solely endothermal. Dissolution heat of peaks A + B from this work and from ref. [17] have been correlated with the corresponding YS in Figure 3c. It becomes obvious that for all investigated aging parameters the dissolution heat of peaks A + B and the YS increase after stress aging. Therefore, the higher YS and UTS of stress-aged specimens compared to those of conventionally aged counterparts (cf. Table 2) can be rationalized by the higher fraction of strengthening precipitates. Dissolution heat of peaks A + B could not be properly evaluated after stress aging at 200 MPa and 120 °C for 24 h, because the cumulative DSC curve shows no clear finish temperature of dissolution peak B.

Bright-field (BF) and dark-field (DF) STEM micrographs of the as-received (T6) specimen are shown in Figure 4. The GB precipitates (η), which resulted in the formation of PFZs, are present

in the microstructure of the as-received specimen. Formation of PFZs can be related to the migration of the alloying elements from the surrounding to assist the growth of the GB precipitates.^[12] The width of the PFZ was measured to be about 20 nm. Furthermore, as a result of the T6 heat treatment, in the grain interior fine and dispersed η' are formed.

BF and DF STEM micrographs of the specimen aged at 120 °C for 24 h at 200 MPa are shown in Figure 5. At lower magnifications, dislocation tangles are evident (cf. Figure 5a–d). Dislocation tangles observed in the microstructure of this stress-aged specimen may stem from the presence of external stress during aging (cf. Figure 5a,b). As discussed earlier, the presence of a stress of 200 MPa during aging at 120 °C can lead to dislocation multiplication. It is also worth noting that some pile-ups are formed in the vicinity of GBs (cf. Figure 5c,d). It was previously reported that GBs are effective obstacles to dislocation motion in high-strength Al alloys.^[43] Images captured at higher magnifications provide more information about second-phase particles formed within the grain interior and along the GBs. It is evident that stress aging could not fully eliminate PFZs in the vicinity of the GBs (cf. Figure 5e,f). However, the width of the PFZ was measured to be even less than 15 nm

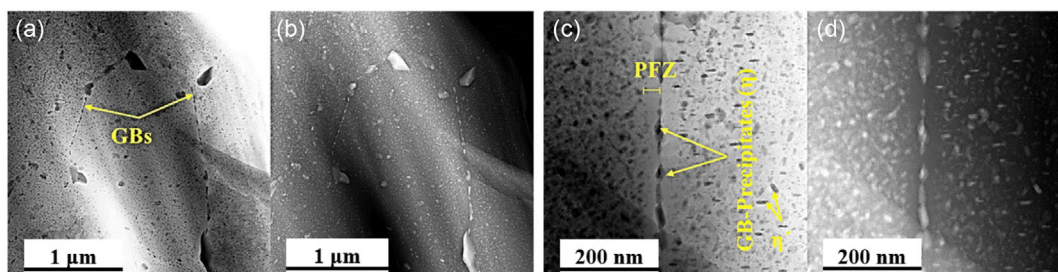


Figure 4. a,c) BF and b,d) DF STEM images of the as-received (T6) specimen. GBs and precipitates are marked by yellow arrows. GB-precipitates (η) and fine and dispersed η' in the grain interior can be observed.

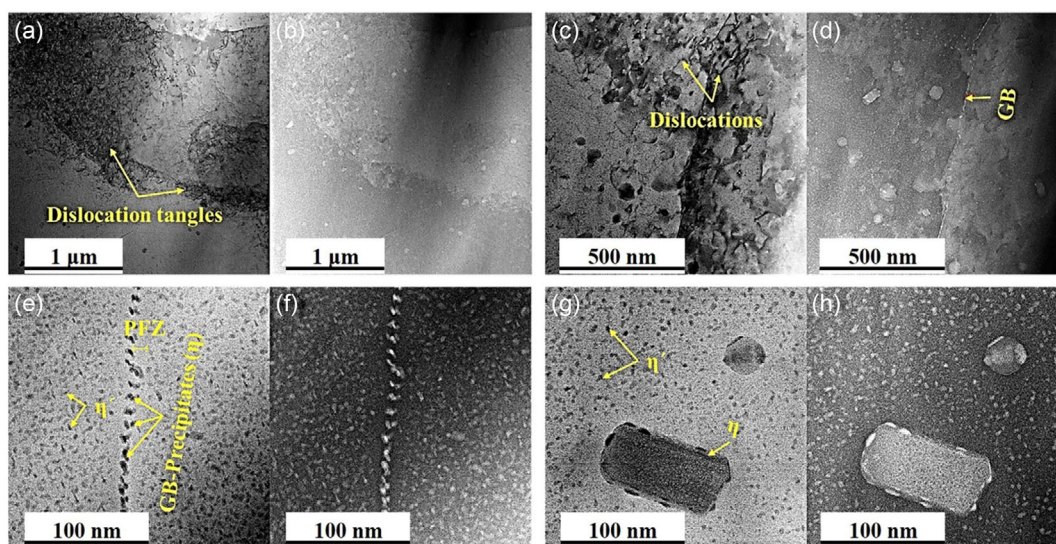


Figure 5. a,c,e,g) BF and b,d,f,h) DF STEM images of the specimen aged at 120 °C for 24 h at 200 MPa. GBs, dislocations, and precipitates are marked by yellow arrows. GB precipitates (η), dislocation tangles, and fine and dispersed η' in the grain interior can be seen in this condition.

which is narrower than that measured in the as-received (T6) counterpart (about 20 nm). The formation of such narrow PFZs can be attributed to additional nucleation sites for precipitations in the stress-aged specimens. This observation was double checked in different regions. The η' precipitates were captured in the grain interior, while some coarse η precipitates were detected in both the grain interior and along the GBs. The sizes of η' and η precipitates observed (cf. Figure 5g,h) are less than 10 nm and larger than 50 nm, respectively.

BF STEM and corresponding EDS elemental mappings of the specimen aged at 120 °C for 24 h at a stress of 200 MPa are shown in Figure 6. EDS analysis indicates that GB precipitates are rich in Mg and Zn. It was reported that GB precipitates represent η precipitates with the stoichiometry of $MgZn_2$.^[44] Fine and dispersed precipitates in the grain interior are also rich in Mg and Zn. These fine precipitates are presumably η' precipitates featuring a stoichiometry of $MgZn$.^[44]

3.3. Mechanical Properties Under Cyclic Loading

CDRs of conventionally aged and stress-aged specimens obtained at different total strain amplitudes are displayed in Figure 7. Scatter in LCF is less pronounced. Regardless of material conditions, an increase in stress amplitudes and a decrease in fatigue life can be observed with an increase in the total strain amplitude. Due to an increasing total strain amplitude, fatigue crack nucleation and propagation can be promoted.^[36,45,46] At total strain amplitudes of $\Delta\epsilon_t/2 = \pm 0.4\%$ and $\Delta\epsilon_t/2 = \pm 0.6\%$, cyclic stability with no traces of cyclic hardening and softening is evident. However, an interesting cyclic hardening can be observed for the specimens being conventionally and stress-aged for a short time (2 h) during fatigue at a total strain amplitude of $\Delta\epsilon_t/2 = \pm 0.8\%$. The condition of the specimens aged for 2 h can be considered as an underaged condition. Mechanical properties of this condition obtained under monotonic loading already indi-

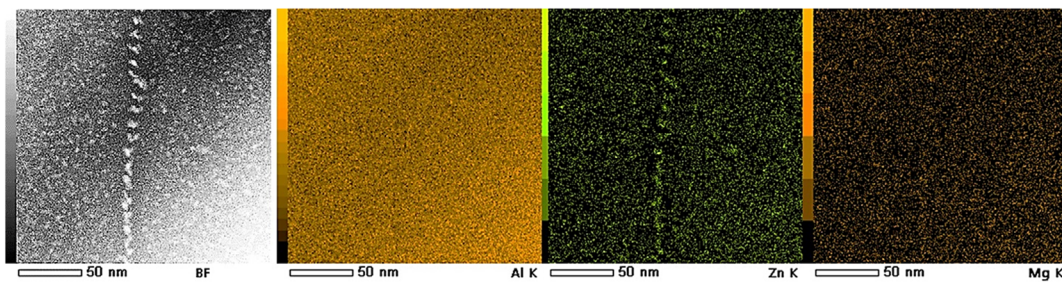


Figure 6. BF STEM and corresponding EDS elemental mapping of the specimen aged at 120 °C for 24 h under a stress of 200 MPa; a single GB, PFZs, and the grain interior depicting their corresponding chemical composition analysis can be seen in this figure. Precipitates were found to be rich in Mg and Zn alloying elements.

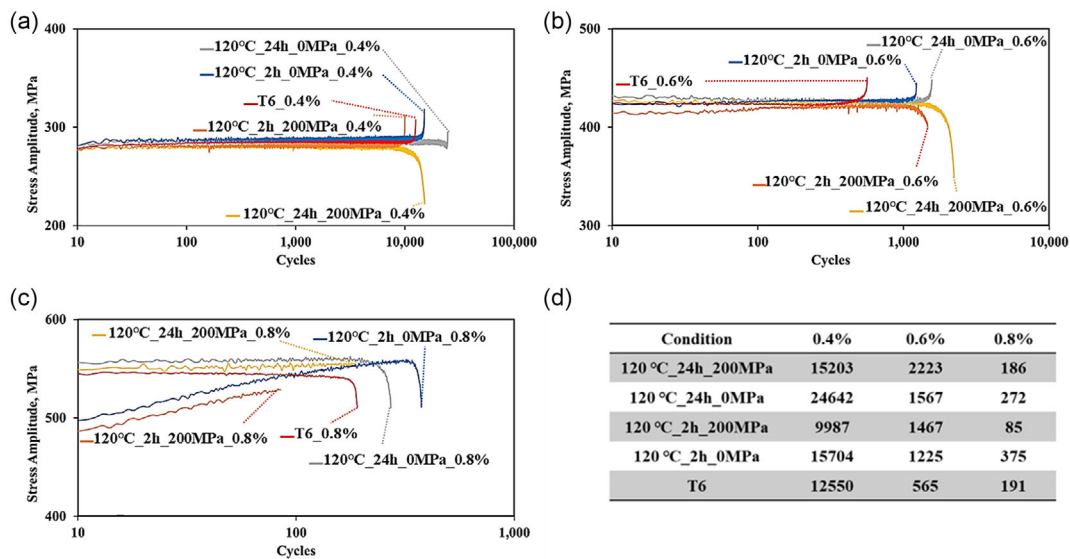


Figure 7. CDRs of EN AW-7075 in various conditions fatigued at different total strain amplitudes of a) $\Delta\epsilon_t/2 = \pm 0.4\%$, b) $\Delta\epsilon_t/2 = \pm 0.6\%$, and c) $\Delta\epsilon_t/2 = \pm 0.8\%$; d) total specimen lifetime (cycles to failure) for all LCF experiments carried out. Information on the actual condition and the total strain amplitude applied is provided in each subimage. Increasing stress amplitudes and decreasing specimen lifetime can be seen with an increase in strain amplitude. A considerable cyclic hardening can be observed in case of the specimens being conventionally and stress aged for a short time (2 h) during fatigue at a total strain amplitude of $\Delta\epsilon_t/2 = \pm 0.8\%$.

cated that the specimens aged for 2 h feature an underaged condition as they were characterized by reduced hardness and strength values. During cyclic deformation of underaged Al alloys, dynamic strain aging (DSA) may occur, resulting in cyclic hardening.^[47] At a total strain amplitude of $\Delta\epsilon_t/2 = \pm 0.8\%$, the strain level, that is, the actual level of plastic strain, seems to be high enough to promote the DSA phenomenon. In case of the DSA phenomenon, due to the formation of vacancies during cyclic deformation, highly mobile solute atoms (Mg and Zn) can diffuse from the SSS to pin dislocations in the underaged specimens. Furthermore, GP zones can also be formed in an underaged Al alloy with an increase in the concentration of vacancies and diffusion of solute atoms during cyclic deformation.^[48,49] Therefore, DSA and an increase in the volume fraction of GP zones can be responsible for the cyclic hardening observed for the specimens aged for 2 h in the present study. For the specimens aged for a longer time of 24 h, neither cyclic hardening nor cyclic softening can be observed. The absence of cyclic hardening or softening indicates merely elastic deformation and/or concurrent generation and cancellation of dislocations.^[36] The impact of external stress during aging on the CDRs is not pronounced. In

the following section, the microstructural evolution is elaborated using TEM studies following the fatigue experiments.

It should also be worth noting that the stress amplitudes are slightly lower in the stress-aged specimens compared to those in the conventionally aged counterparts. This may be imputed to the difference in the dislocation densities and the alignment of precipitates in the stress-aged specimens. In the final subsection, these aspects are schematically discussed.

Figure 8 shows half-life hysteresis loops of EN AW-7075 in various conditions plotted in relative coordinates. Relative stress and strain values were calculated from the actual values in order to plot the start and end points of the half-life hysteresis loops in the origin (0, 0). With an increase in total strain amplitude, hysteresis loops are more open, indicating a higher energy dissipation per cycle and, eventually, dislocation generation.^[36] By comparing different material conditions, it can be deduced that specimens aged for 24 h show narrower hysteresis loops indicating superior fatigue performance. After the hysteresis loops are plotted in relative coordinates, the Masing/non-Masing behavior of different conditions can also be evaluated. The Masing/non-Masing behavior of specimens aged for 24 h can only hardly be discussed as these conditions are characterized by narrow and

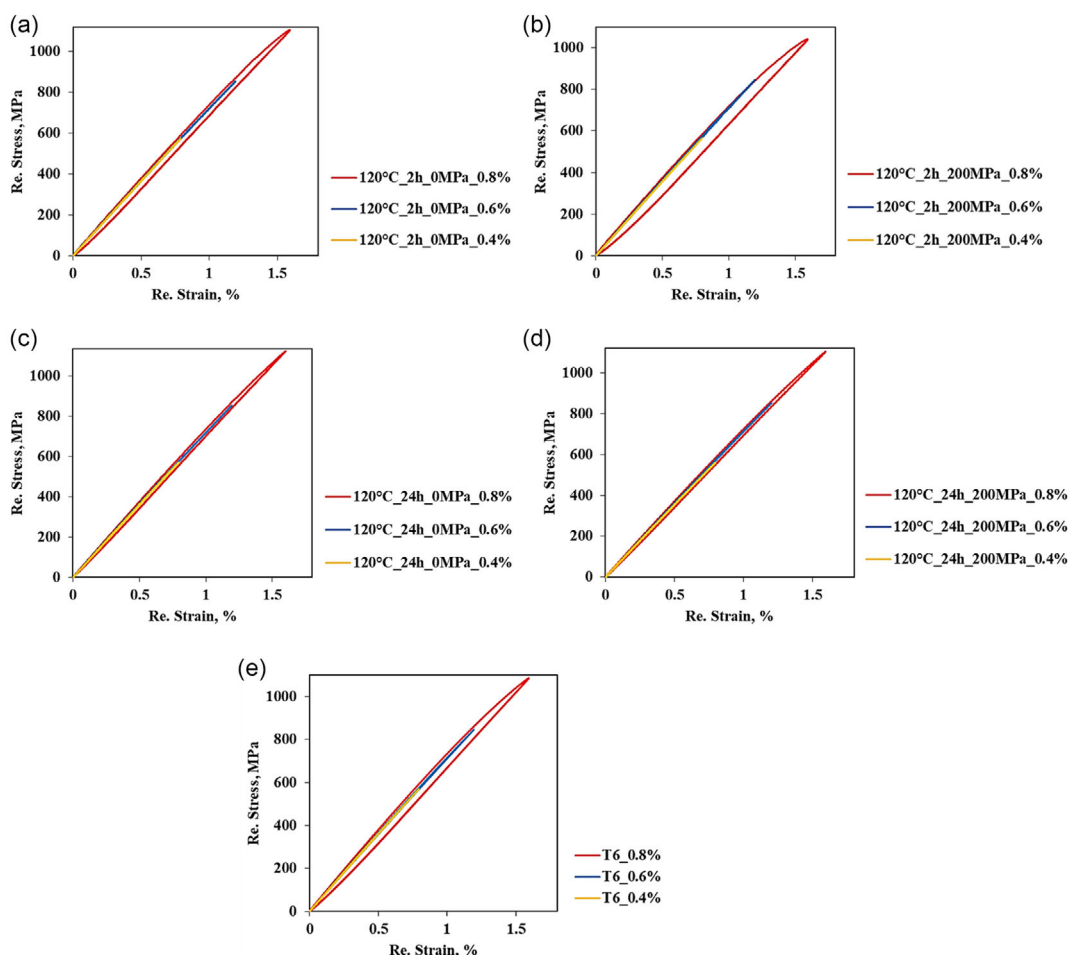


Figure 8. Half-life hysteresis loops of a) 120 °C_2 h_0 MPa, b) 120 °C_2 h_200 MPa, c) 120 °C_24 h_0 MPa, d) 120 °C_24 h_200 MPa, and e) T6. All hysteresis loops are plotted in relative coordinates of stress and strain. With an increase in total strain amplitude, hysteresis loops reveal an increased contribution of plastic strain.

elastic hysteresis loops at all strain amplitudes considered. For the specimens aged for 2 h, a perfect Masing behavior cannot be observed. This leads to the conclusion that severe dislocation activity, depending on the actual loading amplitude, is taking place.^[50,51] The effect of external stress during aging on the shape and characteristics of hysteresis loops is not significant. However, half-life hysteresis loops of stress-aged specimens (especially at higher strain amplitudes) seem to be slightly wider than those of conventionally aged counterparts. By comparing results obtained in quasistatic and cyclic regimes, it can be concluded that stress aging allows for the improvement of the monotonic mechanical properties of this alloy without deteriorating the alloy performance in the LCF regime. Since the highest accumulated plastic strains are applied to the material in the LCF regime, cyclic microstructural stability of a given condition is stressed to the highest degree possible.

A comprehensive three-parameter model based on hysteresis energy has been recently developed for an Al–Si alloy in order to predict fatigue life in the LCF regime.^[52] This model proposes an appropriate form of a criterion for fatigue damage evaluation.

Experimental results obtained herein can also be used to predict and evaluate fatigue life in the LCF regime. However, the present study is focused on the effect of superimposed stress on the cyclic properties of the EN AW 7075 alloy using LCF experiments. Therefore, the elaboration of a fatigue damage criterion and assessment of the fatigue life is beyond the scope of the present research work and, thus, will be addressed in a follow-up study.

3.4. Microstructural Evolution upon Cyclic Deformation

BF and DF STEM images of the specimen aged at 120 °C for 2 h at 200 MPa and fatigued at $\Delta\epsilon_t/2 = \pm 0.8\%$ are shown in **Figure 9**. At lower magnifications, dislocation tangles and coarse η precipitates can be observed. It is difficult to conclude whether dislocation tangles are formed due to cyclic deformation or previous stress aging treatment. At higher magnifications, not only η precipitates but also η' precipitates can be seen in the grain interior. Basically, fine η' precipitates are responsible for strengthening of

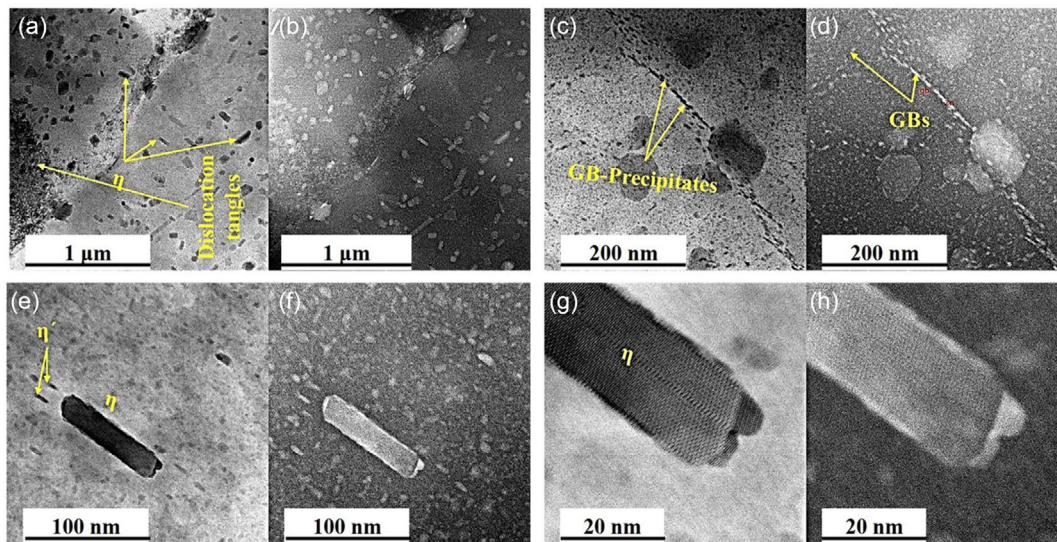


Figure 9. a,c,e,g) BF and b,d,f,h) DF STEM images of the specimen aged at 120 °C for 2 h at 200 MPa and fatigued at $\Delta\epsilon_t/2 = \pm 0.8\%$. GBs, dislocations, and precipitates are marked by yellow arrows. GB precipitates (η), dislocation tangles, and fine and dispersed η' precipitates in the grain interior can be seen for this specimen.

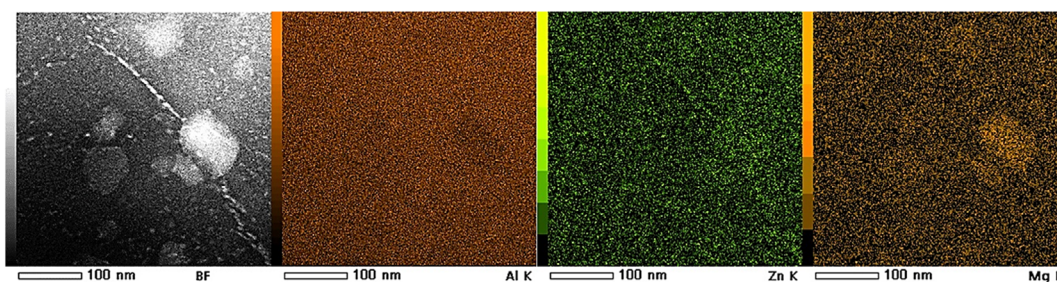


Figure 10. BF STEM and corresponding EDS elemental mapping of the specimen aged at 120 °C for 2 h at 200 MPa and fatigued at $\Delta\epsilon_t/2 = \pm 0.8\%$; a single GB, PFZs, and the grain interior depicting their corresponding chemical composition analysis can be seen in this figure. Precipitates were found to be rich in Mg and Zn.

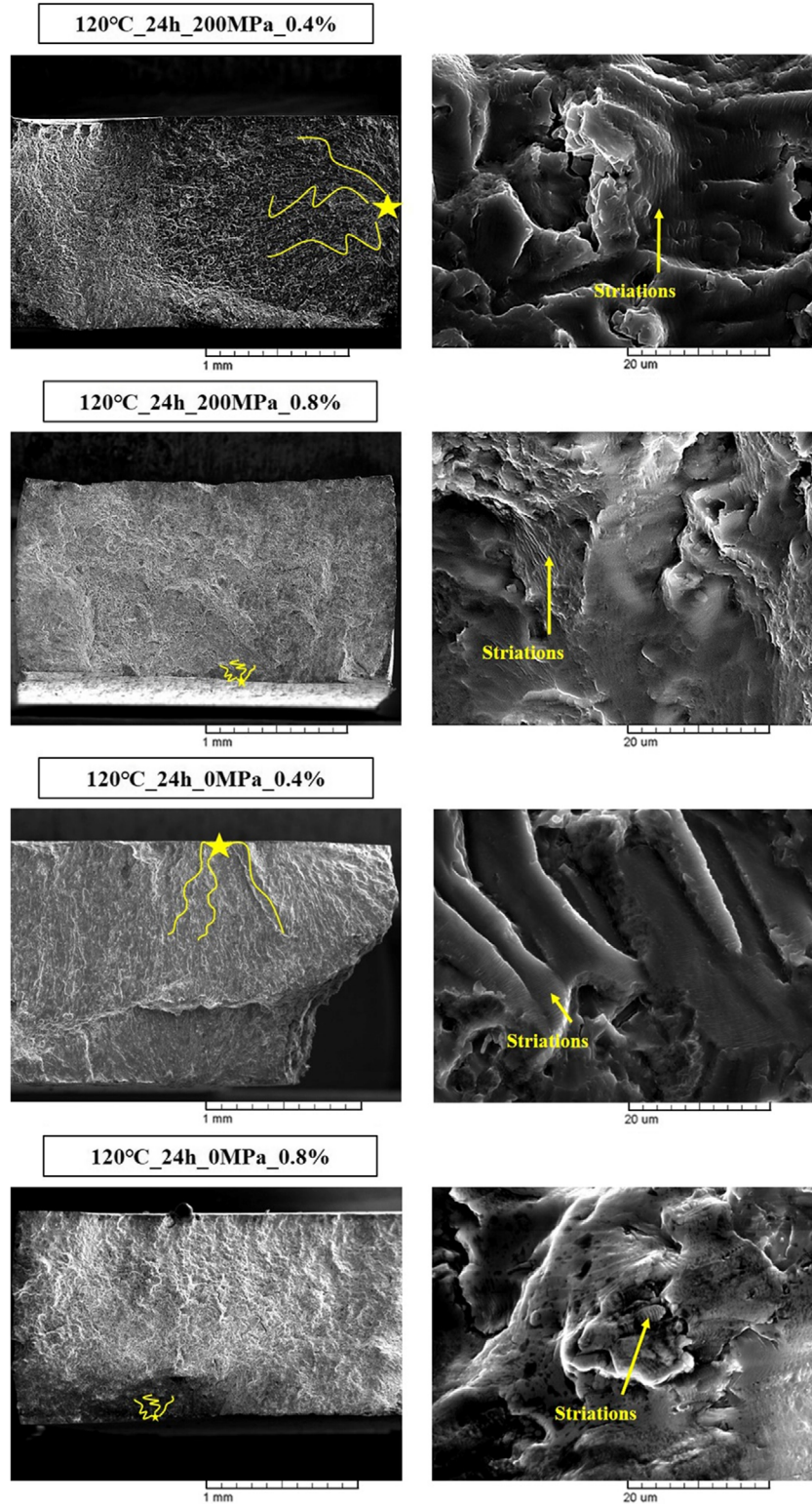


Figure 11. Fracture surfaces of conventionally and stress-aged specimens upon cyclic deformation at different strain amplitudes. Yellow traces schematically indicate fatigue crack nucleation and growth. Striations are marked by yellow arrows. Fatigue cracks were initiated close to the subsurface layers. A larger crack propagation area can be observed for the specimens fatigued at a lower strain amplitude of $\Delta\epsilon_t/2 = \pm 0.4\%$. Higher-magnification micrographs of the fracture surfaces are shown to the right.

this alloy.^[17] Fatigue-induced microstructure changes have not yet been resolved by STEM.

The specimen aged at 120 °C for 2 h under a stress of 200 MPa and fatigued at $\Delta\epsilon_f/2 = \pm 0.8\%$ was also studied via EDS elemental mapping, as shown in **Figure 10**. Similar to the stress-aged specimens before cyclic loading, GB precipitates and fine precipitates in the grain interior are rich in Zn and Mg, pointing at the formation of η' (MgZn₂) and η (MgZn) precipitates, respectively.

3.5. Fracture Analysis

Fracture surfaces of selected conventionally and stress-aged specimens upon cyclic deformation at total strain amplitudes of $\Delta\epsilon_f/2 = \pm 0.4\%$ and $\Delta\epsilon_f/2 = \pm 0.8\%$ are shown in **Figure 11**. Evidently, fatigue cracks were initiated near the subsurface layers. Nucleation of cracks from near-surface layers can be related to cyclic slip irreversibility.^[36,53,54] During forward loading, many dislocations appear at the free surface of the specimen and afterward, they do not return into the material in the reverse loading direction and, thus, leave irreversible slip behind. Accumulation of irreversible slip can cause the formation of defects and, hence, crack initiation from subsurface layers. Generally, fracture surfaces shown reveal well-known features of a fatigued specimen, that is, areas of fatigue crack initiation and propagation (featuring submicrometer fatigue striations), as well as an overload final fracture region. It is also worth noting that a larger crack propagation area can be observed for the specimens fatigued at a lower strain amplitude of $\Delta\epsilon_f/2 = \pm 0.4\%$. This could be related to the low fatigue crack propagation rate at a lower strain amplitude.^[36] Besides, the fatigue crack propagation rate can be traced by the striations observed at higher magnifications. By comparing fracture surfaces of conventionally and stress-aged specimens upon cyclic deformation, it can be deduced that the appearances of the fracture surfaces of both conditions are very similar to each other. This observation is in line with the almost identical mechanical properties in the examined regime.

3.6. Process–Property–Microstructure Relationships

For a better understanding of the results presented, the relationships between process, microstructure, and property are schematically summarized in **Figure 12**. Results obtained in the present study revealed that the aging time has a substantial effect on the microstructure and LCF behavior of the EN AW 7075 alloy. As discussed earlier, cyclic hardening occurred during the cyclic deformation of this alloy in the underaged condition (2 h). Such cyclic hardening can be linked to the DSA phenomenon. As schematically detailed, highly mobile solute atoms of Mg and Zn can segregate around dislocations in the underaged condition. Thus, these solute atoms pin dislocations and impede their motions.^[48,49] On the other hand, after a longer aging time of 24 h, a higher volume fraction of precipitates can be formed compared to those aged for only 2 h. Thus, the amount of solute atoms in the matrix of specimens aged for 24 h is considerably reduced compared to those aged for 2 h. Taking these points into consideration, dislocation–precipitate interactions are expected to govern mechanical properties in the specimens aged for 24 h.

The effect of the presence of external superimposed stress during aging on the microstructure, CDRs, and hysteresis loops of EN AW 7075 alloy is schematically displayed in **Figure 13**. Results obtained in the present study indicate that the stress amplitude values were slightly lower for the stress-aged specimens in comparison to the conventionally aged counterparts. Besides, the half-life hysteresis loops of the stress-aged specimens are relatively wider than those of the conventionally aged specimens, eventually indicating a higher share of plastic deformation per cycle in the stress-aged condition. From a microstructural perspective and the experimental analysis in the present study (**Figure 5**), stress-aged specimens are supposed to have a higher dislocation density before the start of cyclic deformation. As mentioned earlier, the presence of external superimposed stress during aging at 120 °C is expected to cause dislocation multiplication.^[19] It should also be noted that the presence of superimposed stress can also result in a preferential alignment of precipitates.^[20,55] The aligned precipitates may facilitate

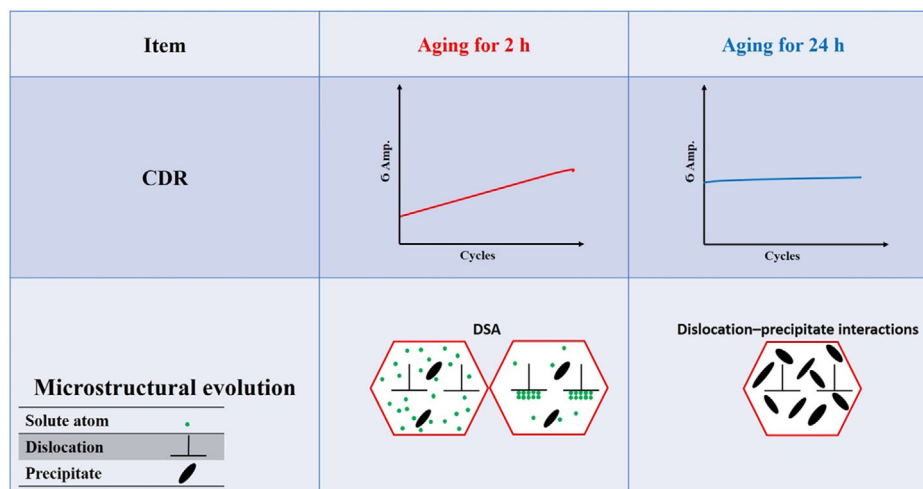


Figure 12. Schematic illustration highlighting the effect of aging time on the CDR and microstructural evolution of EN AW 7075. Differences in the CDRs of specimens aged for 2 and 24 h are highlighted. The DSA phenomenon and dislocation–precipitate interactions in a grain are highlighted.

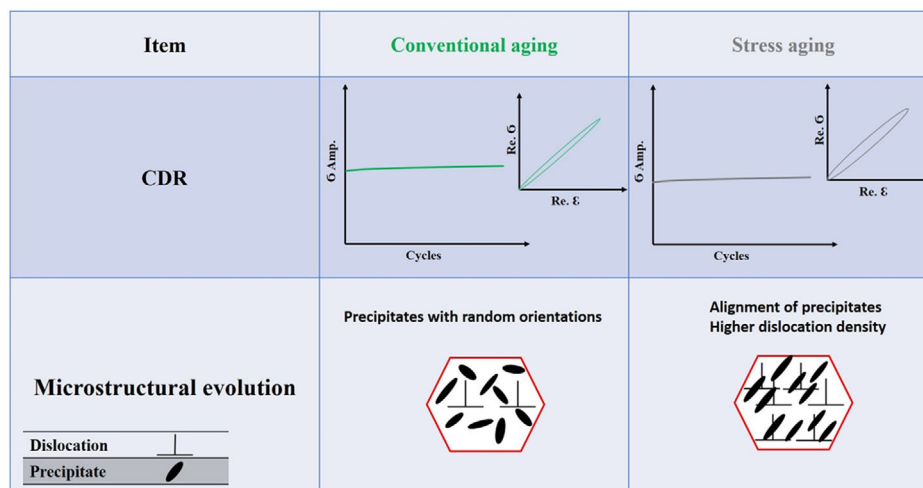


Figure 13. Schematic illustration highlighting the effect of presence of external superimposed stress during aging on the CDRs, hysteresis loops, and microstructure of the EN AW 7075 alloy.

dislocation motion during cyclic loading.^[56] The formation of parallel precipitates during aging under stress might be the main reason for the higher cyclic plastic deformation per cycle and lower stress amplitudes in stress-aged specimens. For experimental proof of the presence of aligned precipitates, in-depth microstructural studies via high-resolution TEM have to be carried out in follow-up studies.

4. Conclusion

In the present study, mechanical properties of conventionally and stress-aged EN AW-7075 were investigated under monotonic and cyclic loading in the LCF regime. The following conclusions can be drawn. 1) By comparing the results of conventionally and stress-aged specimens, it can be concluded that aging under superimposed external stress could improve the mechanical properties of EN AW-7075 alloy. Superimposed external stress accelerates the precipitation kinetics. 2) BSE analysis revealed the formation and growth of precipitates in the matrix. STEM studies showed that superimposed external stress could lead to the formation of a higher fraction of strengthening η' precipitates. The formation of η precipitates was observed both in the grain interior and along the GBs, while η' precipitates were only formed in the grain interior. The width of the PFZ in the stress-aged specimen was measured to be less than 15 nm, thus, smaller than in the reference condition. 3) Stress aging causes significantly larger dissolution peaks A (GP-zones) and B (η') in subsequent DSC heating experiments compared to stressless aging. Thus, a higher fraction of strengthening precipitates have been formed during stress aging. Dissolution heat of peaks A + B could be correlated with the YS. 4) CDRs and half-life hysteresis loops of conventionally and stress-aged EN AW-7075 alloy revealed that regardless of the material condition, the stress amplitude and energy dissipation were increased and fatigue life was degraded with an increase in strain amplitude. Cyclic hardening observed for the specimens aged for 2 h at the highest total

strain amplitude considered ($\Delta\epsilon_t/2 = \pm 0.8\%$) was attributed to DSA. Stress amplitudes of specimens aged with the presence of superimposed stress were found to be marginally lower than those aged conventionally. Hysteresis loops of stress-aged specimens were slightly wider than those of conventionally aged counterparts. 5) Based on the results presented, stress aging allows to improve the monotonic mechanical properties of EN AW-7075 without deteriorating the alloy performance in the LCF regime. As the LCF regime is characterized by highest accumulated plastic strains, fatigue crack advance is thought to be of higher importance than crack initiation. Under these loading conditions, cyclic microstructural stability of a given condition is stressed to the highest extent possible. Future work will address fatigue regimes being dominated by crack initiation.

Acknowledgements

The authors gratefully acknowledge financial support from the Hessen State Ministry for Higher Education, Research and the Arts—Initiative for the Development of Scientific and Economic Excellence (LOEWE) for Project ALLEGRO (Subproject B1). J.Z. acknowledges support from ARRS, P1-0417, and J2-4440.

Open Access funding enabled and organized by Projekt DEAL.

Conflict of Interest

The authors declare no conflict of interest.

Author Contributions

S.V.S.: took care of conceptualization, methodology, data curation, investigation, writing the original draft, and writing the review and editing; P.K.: took care of conceptualization, methodology, investigation, and writing the review and editing; M.K.: took care of methodology, data curation, investigation, and writing the review and editing; T.W.: took care of methodology, investigation, and writing the review and editing; A.H.: took care of methodology, investigation, and writing the review and editing; H.F.:

took care of methodology, investigation, data curation, and writing the review and editing; J.Z. took care of data curation, investigation, and writing the review and editing; O.K.: took care of resources, project administration, writing the review and editing, and supervision; T.N.: took care of conceptualization, resources, project administration, writing the review and editing, and supervision.

Data Availability Statement

The data that support the findings of this study are available from the corresponding author upon reasonable request.

Keywords

high-strength aluminum alloys, low-cycle fatigue, mechanical properties, microstructures, stress aging

Received: January 20, 2023

Revised: May 3, 2023

Published online: May 25, 2023

-
- [1] A. Gesing, R. Wolanski, *JOM* **2001**, 53, 21.
 [2] N. R. Harrison, S. G. Luckey, *SAE Int. J. Mater. Manuf.* **2014**, 7, 2014.
 [3] L.-T. Li, Y. C. Lin, H.-M. Zhou, Y.-Q. Jiang, *Comput. Mater. Sci.* **2013**, 73, 72.
 [4] K. Senthil, M. A. Iqbal, P. S. Chandel, N. Gupta, *Int. J. Impact Eng.* **2017**, 108, 171.
 [5] J. Decke, A. Engelhardt, L. Rauch, S. Degener, S. V. Sajadifar, E. Scharifi, K. Steinhoff, T. Niendorf, B. Sick, *Crystals* **2022**, 12, 1281.
 [6] Y. Xu, Z. Zhang, Z. Gao, Y. Bai, P. Zhao, W. Mao, *Mater. Charact.* **2021**, 182, 111559.
 [7] E. Georgantzia, M. Gkantou, G. S. Kamaris, *Eng. Struct.* **2021**, 227, 111372.
 [8] Y. Li, Z. R. Zhang, Z. Y. Zhao, H. X. Li, L. Katgerman, J. S. Zhang, L. Z. Zhuang, *Metall. Mater. Trans. A* **2019**, 50, 3603.
 [9] J. Lu, Y. Song, L. Hua, K. Zheng, D. Dai, *J. Alloys Compd.* **2018**, 767, 856.
 [10] Y. Liu, Z. Zhu, Z. Wang, B. Zhu, Y. Wang, Y. Zhang, *Procedia Eng.* **2017**, 207, 723.
 [11] M. Tisza, I. Czinege, *Int. J. Lightweight Mater. Manuf.* **2018**, 1, 229.
 [12] S. V. Sajadifar, G. Moieni, E. Scharifi, C. Lauhoff, S. Böhm, T. Niendorf, *J. Mater. Eng. Perform.* **2019**, 28, 5255.
 [13] S. V. Sajadifar, E. Scharifi, U. Weidig, K. Steinhoff, T. Niendorf, *Metals* **2020**, 10, 884.
 [14] S. V. Sajadifar, E. Scharifi, U. Weidig, K. Steinhoff, T. Niendorf, *HTM J. Heat Treat. Mater.* **2020**, 75, 177.
 [15] A. Karaaslan, I. Kaya, H. Atapek, *Met. Sci. Heat Treat.* **2007**, 49, 443.
 [16] M. F. Ibrahim, A. M. Samuel, S. A. Alkahtani, F. H. Samuel, *Miner. Met. Mater. Ser.* **2016**, 383.
 [17] S. V. Sajadifar, P. Krooß, H. Fröck, B. Milkereit, O. Kessler, T. Niendorf, *Metals* **2021**, 11, 1142.
 [18] Y. C. Lin, Y.-Q. Jiang, J.-L. Zhang, X.-M. Chen, *Adv. Eng. Mater.* **2018**, 20, 1700583.
 [19] M. Kolar, K. O. Pedersen, S. Gulbrandsen-Dahl, K. Marthinsen, *Trans. Nonferrous Met. Soc. China* **2012**, 22, 1824.
 [20] A. W. Zhu, E. A. Starke, *Acta Mater.* **2001**, 49, 2285.
 [21] E. Scharifi, U. Savaci, Z. B. Kavaklioglu, U. Weidig, S. Turan, K. Steinhoff, *Mater. Charact.* **2021**, 174, 111026.
 [22] T. Minh Ngo, T. Thi Van Nguyen, H. Thi To Phung, T. Liu, R. Su, Y. Qu, R. Li, *Mater. Res. Express* **2018**, 5, 116526.
 [23] M. Orłowska, E. Ura-Birńczyk, L. Śniezek, P. Skudniewski, M. Kulczyk, B. Adamczyk-Cieślak, K. Majchrowicz, *Materials* **2022**, 15, 4343.
 [24] M. Fourmeau, C. D. Marioara, T. Børvik, A. Benallal, O. S. Hopperstad, *Philos. Mag.* **2015**, 95, 3278.
 [25] C. Schick, V. Mathot, *Fast Scanning Calorimetry*, Springer International Publishing, Switzerland **2016**.
 [26] J. Osten, B. Milkereit, C. Schick, O. Kessler, *Materials* **2015**, 8, 2830.
 [27] M. Liu, Z. Wu, R. Yang, J. Wei, Y. Yu, P. C. Skaret, H. J. Roven, *Prog. Nat. Sci. Mater. Int.* **2015**, 25, 153.
 [28] M. P. Liu, T. H. Jiang, J. Wang, Q. Liu, Z. J. Wu, Y. Da Yu, P. C. Skaret, H. J. Roven, *Trans. Nonferrous Met. Soc. China* **2014**, 24, 3858.
 [29] J. Osten, C. Lux, B. Milkereit, M. Reich, O. Kessler, *Mater. Sci. Forum* **2016**, 877, 159.
 [30] W. B. Shou, D. Q. Yi, H. Q. Liu, C. Tang, F. H. Shen, B. Wang, *Arch. Civ. Mech. Eng.* **2016**, 16, 304.
 [31] L. Winter, K. Hockauf, S. Winter, T. Lampke, *Mater. Sci. Eng., A* **2020**, 795, 140014.
 [32] L. Leng, Z. J. Zhang, Q. Q. Duan, P. Zhang, Z. F. Zhang, *Mater. Sci. Eng., A* **2018**, 738, 24.
 [33] L. G. Hou, W. L. Xiao, H. Su, C. M. Wu, D. G. Eskin, L. Katgerman, L. Z. Zhuang, J. S. Zhang, *Int. J. Fatigue* **2021**, 142, 105919.
 [34] R. Branco, J. D. Costa, L. P. Borrego, S. C. Wu, X. Y. Long, F. V. Antunes, *Eng. Fail. Anal.* **2020**, 114, 104592.
 [35] V. Pandey, K. Chattopadhyay, N. C. Santhi Srinivas, V. Singh, *Int. J. Fatigue* **2017**, 103, 426.
 [36] S. V. Sajadifar, E. Scharifi, T. Wegener, M. Krochmal, S. Lotz, K. Steinhoff, T. Niendorf, *Int. J. Fatigue* **2022**, 156, 106676.
 [37] S. M. Ghalebandi, A. Fallahi-Arezodar, H. Hosseini-Toudeshky, *Fatigue Fract. Eng. Mater. Struct.* **2016**, 39, 1517.
 [38] A. H. Feng, D. L. Chen, Z. Y. Ma, *Metall. Mater. Trans. A* **2010**, 41, 957.
 [39] H. Fröck, M. Reich, B. Milkereit, O. Kessler, *Materials* **2019**, 12, 1085.
 [40] S. V. Emani, J. Benedyk, P. Nash, D. Chen, *J. Mater. Sci.* **2009**, 44, 6384.
 [41] D. J. Lloyd, M. C. Chaturvedi, *J. Mater. Sci.* **1982**, 17, 1819.
 [42] S. Liu, Q. Li, H. Lin, L. Sun, T. Long, L. Ye, Y. Deng, *Mater. Des.* **2017**, 132, 119.
 [43] K. Hockauf, M. F.-X. Wagner, T. Halle, T. Niendorf, M. Hockauf, T. Lampke, *Acta Mater.* **2014**, 80, 250.
 [44] R. Goswami, S. Lynch, N. J. H. Holroyd, S. P. Knight, R. L. Holtz, *Metall. Mater. Trans. A* **2013**, 44, 1268.
 [45] S. V. Sajadifar, G. G. Yapici, E. Demler, P. Krooß, T. Wegener, H. J. Maier, T. Niendorf, *Int. J. Fatigue* **2019**, 122, 228.
 [46] C. W. Shao, P. Zhang, R. Liu, Z. J. Zhang, J. C. Pang, Q. Q. Duan, Z. F. Zhang, *Acta Mater.* **2016**, 118, 196.
 [47] M. Hörnqvist, B. Karlsson, *Mater. Sci. Eng., A* **2008**, 479, 345.
 [48] W. Z. Han, Y. Chen, A. Vinogradov, C. R. Hutchinson, *Mater. Sci. Eng., A* **2011**, 528, 7410.
 [49] S. Mohammed, S. Gupta, D. Li, X. Zeng, D. Chen, *Materials* **2020**, 13, 4115.
 [50] T. Niendorf, T. Wegener, Z. Li, D. Raabe, *Scr. Mater.* **2018**, 143, 63.
 [51] T. Niendorf, D. Canadinc, H. J. Maier, *Adv. Eng. Mater.* **2011**, 13, 275.
 [52] M. Wang, J. C. Pang, S. X. Li, Z. F. Zhang, *Mater. Sci. Eng., A* **2017**, 704, 480.
 [53] H. Mughrabi, *Metall. Mater. Trans. B* **2009**, 40, 431.
 [54] A. Weidner, J. Man, W. Tirschlner, P. Klapetek, C. Blochwitz, J. Polák, W. Skrotzki, *Mater. Sci. Eng., A* **2008**, 492, 118.
 [55] H. Hargarter, M. T. Lytle, E. A. Starke, *Mater. Sci. Eng., A* **1998**, 257, 87.
 [56] Z. Y. Song, Q. Y. Sun, L. Xiao, J. Sun, L. C. Zhang, *Mater. Sci. Eng., A* **2011**, 528, 4111.